THESIS FOR THE DEGREE OF LICENTIATE OF ENGINEERING

Experimental study and simulation of sintering of 316L components produced by binder jetting

ALBERTO CABO RIOS

Department of Industrial and Materials Science
CHALMERS UNIVERSITY OF TECHNOLOGY
Gothenburg, Sweden, 2023

Experimental study and simulation of sintering of 316L components produced by binder jetting

ALBERTO CABO RIOS

Technical report no IMS-2023-2

Licentiate Thesis at Chalmers University of Technology

Department of Industrial and Materials Science

Chalmers University of Technology

SE-412 96 Gothenburg

Sweden

Tel: +46 (0)31 772 1000

Printed by Chalmers Reproservice

Gothenburg, Sweden 2023

Experimental study and simulation of sintering of 316L components produced by binder jetting

Alberto Cabo Rios
Department of Industrial and Materials Science
Chalmers University of Technology

Abstract

Binder Jetting (BJT) is a multi-step Additive Manufacturing (AM) technique that is used for producing components with highly complex geometries and competitive final properties with high productivity when compared to other AM technologies. The first step provides the basic part geometric shape (BJT printing), and the next step (debinding and sintering) consolidates the part to reach final geometry and intended basic material properties. Due to the low density of green BJT components after printing (~50-60%), significant shrinkage (~20%) occurs during the sintering process along different directions. Also, sintering may lead to distortion of the external shape of the components.

During BJT printing, the powder is being deposited layer-by-layer and binder is selectively placed to create a 3D geometry. Therefore, the metal particle's arrangement of the green BJT components is influenced by the layer-by-layer buildup nature of the printing process. This impacts the behavior of the components during the debinding and sintering process. The first part of this study aims to develop the understanding of densification development during the sintering of 316L stainless-steel BJT samples. The intensity of the dimensional evolution anisotropy was characterized by multi-axial dilatometry experiments. Measured shrinkages were up to 15% higher along the building direction, while minor variation was found between the other two orthogonal directions. Only small shrinkages (<0.5%) were observed during debinding without significant anisotropy. A rapid increase of the shrinkage rate was observed at high temperature (~1310°C), related to the formation of δ-ferrite phase. This boost of densification is critical to achieve high densities (96-99%) of 316L BJT sintered components. The second part consists of the microstructural evolution analysis. The EBSD phase maps showed the formation of δ-ferrite at temperatures >1300°C. The porosity characterization within different cross-sections demonstrated that some anisotropic distribution of porosity may be developed during sintering.

The last part of this study introduces the application of the continuum theory of sintering for modelling the sintering behavior of 316L BJT components. The identification of model parameters was done from dilatometry data. Then, a new material viscosity expression was proposed to account for the effect of δ-ferrite transformation. The model was proved to accomplish good predictions of the density evolution during sintering of BJT samples.

Keywords: Sintering, binder jetting, dilatometry, anisotropy, additive manufacturing, sintering modelling, 316L stainless steel.

PREFACE

This thesis is based on the work performed at the Department of Industrial and Materials Science at Chalmers University of Technology from June 2019 to July 2021, and in the Powder Technology Laboratory at San Diego State University (SDSU) from August 2021 to June 2022. The work has been carried out under the supervision of Professor Eduard Hryha (Chalmers), Professor Eugene Olevsky (SDSU) and Professor Lars Nyborg as examiner. This work has been performed within the framework of Centre for Additive Manufacture-Metal (CAM²), as an industrial PhD project financed by Digital Metal AB, Höganäs AB and Sandvik AB (until December 2021).

This thesis comprises the introductory part of the project which has been focused on the characterization during the sintering step of 316L stainless-steel parts additively manufactured by binder jetting. Also, initial efforts on the development of a sintering model and the utilization of experimental data were included in this thesis study. Most of the work performed has been summarized and included in the appended papers.

List of appended papers

Paper I: **Sintering anisotropy of binder jetted 316L stainless steel: part I – sintering anisotropy.**
Alberto Cabo Rios, Eduard Hryha, Eugene Olevsky, Peter Harlin, Powder Metallurgy, 2021, 1-10, DOI: https://doi.org/10.1080/00325899.2021.2020485

Paper II: **Sintering anisotropy of binder jetted 316L stainless steel: part II – microstructure evolution during sintering.**
Alberto Cabo Rios, Eduard Hryha, Eugene Olevsky, Peter Harlin, Powder Metallurgy, 2021, 1-13, DOI: https://doi.org/10.1080/00325899.2021.2020486

Paper II: **Modelling of δ-ferrite transformation effect on the sintering behaviour of 316L binder jetted components.**
Alberto Cabo Rios, Eugene A. Olevsky, Eduard Hryha, Mats Persson
WorldPM2022 Conference proceedings, 2022.

Contribution to the appended papers

Paper I: The author planned the study in collaboration with the co-authors. The author performed all the experimental work, except the printing that was performed at Sandvik. The author analyzed the data and wrote the paper in collaboration with the co-authors.

Paper II: The author planned the study in collaboration with the co-authors. The author performed all the experimental work, except the printing and chemical analysis that was conducted at Sandvik. The author analyzed the data and wrote the paper in collaboration with the co-authors.

Paper III: The author planned and performed all the experimental work, except the samples printing that was done at Digital Metal. Analysis of results was performed in collaboration with the co-authors. The author wrote the paper with the help of co-authors.

Table of Contents

Nomenclature

θ	Porosity
V_P	Pore volume
V_T	Total volume
ρ	Density
$\dot{\theta}$	Porosity elimination rate (s^{-1})
$\dot{e}$	Trace of the strain rate tensor (s^{-1})
$\dot{\boldsymbol{\varepsilon}}_{ij}$	Strain rate tensor (s^{-1})
$\boldsymbol{\sigma}_{ij}$	Stress tensor ($N \cdot m^2$)
σ(W)	Equivalent stress rate
W	Equivalent strain rate
φ	Normalized shear modulus
ψ	Normalized bulk modulus
δ_{ij}	Delta de Kronecker
P_L	Sintering stress (Pa)
η_0	Material viscosity ($Pa \cdot s$)
A_0	Viscosity pre-exponential factor ($Pa \cdot s$)
Q	Viscosity activation energy ($J \cdot mol^{-1}$)
R	Gas constant 8.314 ($J \cdot mol^{-1} \cdot K^{-1}$)
T	Temperature (K)
α	Surface energy ($J \cdot m^{-2}$)
r_0	Initial particle mean radius (m)
t	Time (t)
$\dot{G}$	Grain growth rate ($m \cdot s^{-1}$)
G	Grain size diameter (m)
k_0	Grain growth pre-exponential factor ($\mu m^3 \cdot s^{-1}$)
Q_{G}	Grain growth activation energy ($J \cdot mol^{-1}$)
ρ_c	Grain growth critical density
θ_c	Critical porosity fitting parameter
A_1	Piece-wise viscosity pre-exponential factor below T_T ($Pa \cdot s$)
Q_1	Piece-wise viscosity pre-exponential factor above T_T ($Pa \cdot s$)
T_T	Transition temperature (K)
A_2	Piece-wise activation energy below T_T ($Pa \cdot s$)
Q_2	Piece-wise activation energy above T_T ($Pa \cdot s$)

CHAPTER 1: INTRODUCTION

1.1 Background

Additive manufacturing (AM) is defined as a "process of joining materials to make objects from 3D model data, usually layer upon layer, as opposed to subtractive manufacturing methodologies" [1]. Due to its working principle, AM technologies have several advantages like the reduction of wasted material generated during the manufacturing process, reduction of the manufacturing chain process time and the ability to produce highly complex geometries. Most of the metal AM technologies are not utilized for the mass production of components at the moment due to their low productivity or relatively high costs (i.e. laser- or electron-based powder bed fusion). Lately, Binder Jetting (BJT) is being identified as one of the most promising metal AM technologies for mass production in different industries (e.g. automotive, jewelry, etc.) due to its higher productivity and lower costs compared to other AM processes. However, several challenges need to be solved to unlock the full potential of the BJT.

Binder Jetting is a multi-step process in which the powder bed material is selectively glued together by depositing liquid binder to create a green component (printing step). This green state is characterized by its high porosity and poor mechanical properties; thus a secondary step is required to reach the required final properties. Free sintering is typically done by heating the components close to the melting temperature of the metal powder. However, this process induces significant changes at the macro and micro-scale. The parts shrink up to ~20% and shape deformations may occur caused by external forces (i.e. gravity, friction) or heterogenous temperature distributions within the component. Also, the microstructure evolves driven by a combination of diffusional processes during sintering, grain growth and phase transformations, defining the final properties of the components.

Sintering is an ancient process, which has been used for centuries to consolidate ceramic and metallic powdered materials. Thus, extensive knowledge is available on the science of sintering. However, sintering is a complex process highly dependent on many different variables: the powdered material (e.g. chemical composition, particle shape and size distribution), the part shaping process (e.g. injection molding, additive manufacturing) or the sintering process conditions (e.g. time-temperature profile and atmosphere). In BJT, the use of metal powder and sintering processes developed for metal injection molding (MIM) manufacturing is a common practice that results in

good final part properties and reduce development costs. However, the BJT and MIM green components (e.g. density, particle and binder distribution) are totally different because of the green part shaping process. The BJT layer-by-layer powder spreading, and binder deposition process creates a particular heterogeneous particle/porosity structure that may produce anisotropic shrinkages and microstructure evolution during sintering. Also, due to the high temperatures, shape distortions can be significant on the highly complex geometries that can be produced by BJT. Therefore, the ability to predict the BJT components evolution during sintering is a complex but a key factor to unlock the potential of BJT mass production by reducing trial-and-error.

For the simulation of the external geometry evolution during sintering, continuum mechanics sintering models, which can be implemented on finite element methods (FEM) are the most suitable. These models have been developed during the last decades for the prediction of other manufacturing processes like MIM or press and sintering. However, the different characteristics of green BJT components would impact the sintering constitutive relationships required for a detailed prediction. Therefore, first a systematic characterization of the BJT sintering behavior is necessary to address the requirements on modelling of BJT components. This experimental investigation is presented for a 316L stainless steel BJT component in this thesis. Then, the constitutive relationships and methodology for the determination of the materials parameters are studied. Correspondingly, an initial proposal for the modelling of sintering of stainless steel has been developed in the present thesis and future lines of experimental and modelling development have been identified.

1.2 Objectives

The research objectives of this thesis can be differentiated by a thin line that divides the experimental and numerical study of the sintering of components produced by binder jetting additive manufacturing. Experimentally, it is crucial to understand the effect of the green component's characteristic on the sintering behavior and the final properties. Then, the modelling part can be developed based on the theory of sintering together with the experimentally characterized evolution of the BJT components during the sintering process. Some specific questions to be addressed are:

1. ***How the layer-by-layer BJT process relates to the dimensional evolution during the sintering process of stainless steel BJT components?***
2. ***What is the effect of the microstructural evolution on the sintering and modelling of BJT stainless steel components?***

CHAPTER 2: BINDER JETTING METAL ADDITIVE MANUFACTURING

Binder Jetting (BJT) is classified as a multi-step additive manufacturing (AM) process [1], where the first operation provides the basic part geometric shape (BJT printing) and the following consolidates the part to reach final geometry and intended basic material properties (debinding and sintering). The BJT is a process that can be used with different types of powdered materials like polymers, metals or ceramics. However, the study developed in this thesis is focused on metallic alloys and specifically stainless steel 316L. Typically, metal BJT additive manufacturing involves the following main steps: printing, curing, depowdering, debinding and sintering. After printing, the parts have a low relative density (~50-60%) which leads to significant linear shrinkages (~20%) during the densification produced in the sintering step. Also, sintering is typically performed at temperatures close to the melting temperature of the metal powder, which potentially leads to distortions of the external shape of the part geometry. The details of the different metal BJT manufacturing steps and the challenges related to the prediction of the component evolution during the process are discussed in the following sections.

2.1 Binder Jetting Printing

Binder Jetting is an AM method defined as a "process in which a liquid bonding agent is selectively deposited to join powder particles" [1]. During the process, the spreading of a powder layer in a build-box is followed by the deposition of a binder which selectively glue the particles together. This procedure is repeated layer-by-layer to join the powder within the designed three-dimensional geometry in the resulting powder bed. The typical BJT printer system can be divided in several main parts: a binder deposition system, powder dispensing and recoating system, build platform and excess powder collecting chamber as illustrated in Figure 1.

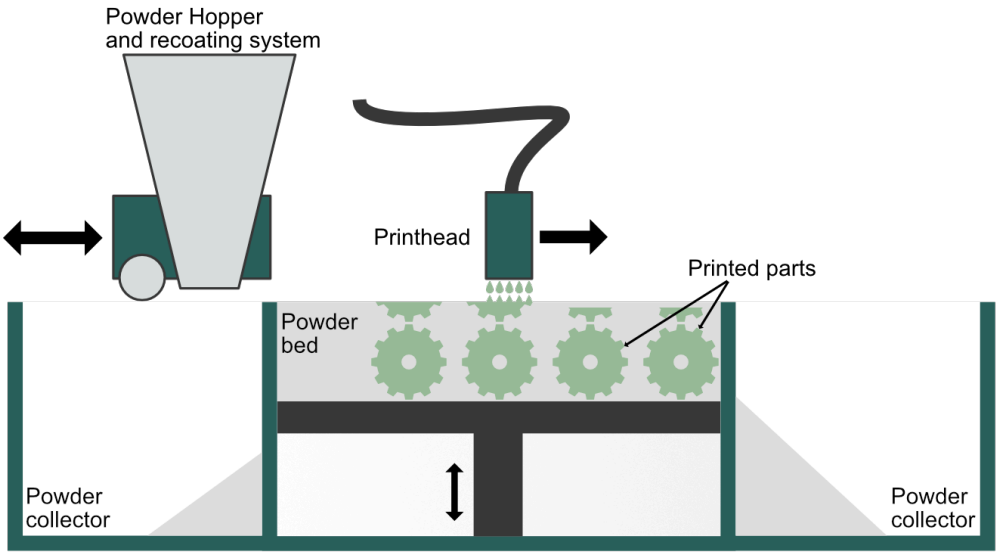

Figure 1. Schematic illustration of the BJT printing process.

Different variations of BJT printer systems can be found in the market, mainly varying the powder bed size, printhead characteristics and powder dispensing and recoating working principles. The operation of these systems can be tuned by different parameters affecting the printing process, green components and ultimately the final sintered components. These variables can be divided in three main groups:

(1) Powder feedstock characteristics.

(2) Powder deposition & spreading.

(3) Binder deposition.

The properties and characteristics of the green component, which embodies the initial condition for the subsequent debinding and sintering steps, is determined by the influence of all these parameters during the BJT printing. Accordingly, the printer mechanisms can be divided in two main systems that must work in unison to achieve the desired printed results: The binder deposition system and the powder spreading and recoating system. The working principles of these mechanisms and the parameters selected for its operation will have a key impact on the particle's arrangement within the printed parts. Figure 2 outlines these main factors that determine the characteristics of the BJT green components.

The powder feedstock is defined by different characteristics as particle morphology, particle size distribution (PSD), powder packing density (tap and apparent density) and the chemical composition (bulk and surface). The powder morphology is an important factor for the printability of the material using BJT. In general, spherical particles are preferred for powder-bed based AM processes due to the good

flowability [2–4], but some recent studies used irregular particles [2,5] (produced by water atomization). Particle size distribution (PSD) is a natural consequence of the atomization process that typically produces a normal (Gaussian) PSD distribution. PSD can be measured using different techniques (e.g. laser diffraction) and is typically represented by the cumulative percentile values D_{10}, D_{50} and D_{90}. Typically, BJT powders mean size may vary from sub-micron sizes to ~100 μm. Smaller powder (<5μm) has higher sintering activity that leads to faster densification, but agglomeration issues may occur during the printing step. In general, larger particles are preferred during the printing process because of its better flowability and higher packing density, while smaller particles are preferred during sintering for faster densification and better final properties. Therefore, a compromise solution needs to be achieved for each specific case. The powder packing density is a property of the powder characteristics. Apparent density is measured on the loose packed particles, whereas tap density is the density of powder that has been tapped, to settle contents, in a container under specified conditions [6]. Due to the absence of any external pressure during printing, the powder bed packing density usually falls in between the apparent and tap density of the powder used.

The powder spreading system is designed to deposit each powder layer within the powder bed. This system has a key impact on the powder bed quality formed during the printing process because it influences the particles arrangement during the printing process. The interaction of the powder material with the system will be mainly influenced by the mechanism design (e.g. blade/roller type) and the particles characteristics. All these features, combined with the operating parameters of the systems (i.e. printing parameters), will determine particle's arrangement within the layer after the spreading step.

The binder deposition system is designed to deposit the liquid binder on the top of each layer to join the selected volume of particles together. The main components are the printhead, the system that moves this printhead and the binder solution used. The impact of binder droplets in the powder bed may cause disturbance on the powder bed [7], so its distribution would be related to the cartridge movement path and binder deposition parameters. The control of these potential defects is crucial for the sintering process, when the evolution of the green parts will be highly influenced by the initial porous green structure. Also, the powder-binder interaction has influence on the geometrical accuracy and final surface roughness of the parts. The binder solution used is also a key component of the BJT manufacturing process, which must meet

some requirements to provide the necessary integrity to the green components without negatively affecting the sintering process and final properties.

After printing, the build-box may be transferred to a furnace where the binder is cured, increasing the strength of the printed (green) parts. In some cases, the curing can be performed in-situ during the printing process. Then, green parts are extracted during depowdering. Finally, the parts are typically consolidated by debinding and sintering in a high-temperature furnace. In some cases, an infiltration process can be done using other material with lower melting point to fill the porosity and consolidate the parts. However, this cannot be used for producing single material components [2]. In this thesis the consolidation is done by sintering of the green components.

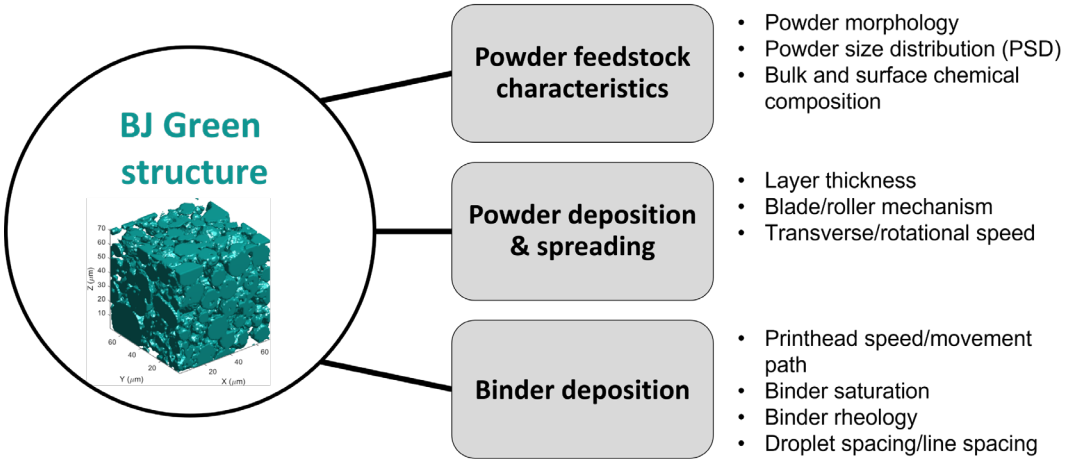

Figure 2. Main factors that determine the characteristics of the BJT green components.

2.2 Debinding

The burnout of the binder within the green components must be produced before the sintering starts. The debinding produces the pyrolysis of the binder component at a relatively low temperature, decomposing and evaporating the binder out of the green component before the sintering process starts. Typically, the debinding process can be done in the same sintering cycle or prior to the sintering step in a separate furnace. The use of polymer in the binder composition may cause carbon residues to remain within the component that could affect the microstructure and phase transformations during the sintering process [8,9]. Previous studies have shown the effect of the carbon residues during the sintering of stainless steel 316L [10]. However, when debinding is properly performed, the amount of these residues is minimized, so their effect is negligible and does not negatively affect the sintering process and final properties of the parts. This, however, strongly depends on the composition of the binder and powder alloy.

Typically, the debinding process is determined by using thermal analysis techniques. For instance, thermogravimetry analysis (TGA) allows for the high precision measurement of the binder removal, including evaporation, decomposition, interaction with the process atmosphere to name some, depicting the binder decomposition kinetics. In the present thesis study, commercial binders are used and the recommended debinding processes from the manufacturers are implemented.

2.3 Sintering

The use of sintering as a process to strength powdered materials is a very ancient process that started with the first produced clay and ceramic pottery back around 24,000 years BC. However, it was not until the 18th century that real quantitative studies were performed to understand the process of sintering [11]. Sintering can be defined as a thermal treatment for bonding particles into a solid structure via mass transport mechanisms. This bonding leads to the densification and the strengthening of the parts during sintering. On the macro-scale, the degree of sintering is commonly expressed by using the relative density. This density is calculated as the fraction between the measured density (in g/cm^3) and the theoretical density of the solid skeleton material. Besides, the porosity is the unfilled space distributed within the powder compact, making the sum of relative density and porosity equal to the unity. As result of the sintering, the external geometry undergoes volumetric shrinkage and the internal microstructure evolution is driven by the pore volume reduction and temperature distribution.

Sintering can be divided depending on the presence of liquid phase during the process as solid-sate sintering (SS), liquid phase sintering (LPS) and super-solid sintering (SLPS). The SS is driven by a combination of diffusion mechanisms that leads to densification without the formation of any liquid phase. On the opposite, LPS is driven by the adherence of solid particles produced by liquid formation [12]. This process is performed using different powder materials, in which one has a substantially lower melting temperature like W-Ni or Fe-Cu alloys. Similarly, in SLPS the densification is promoted by a partial formation of liquid phase. However, in this case pre-alloyed powder is heated to temperatures between the liquidus and solidus to control the solid-liquid fraction [13]. The 316L pre-alloyed powder grades used in this study are typically sintered by solid-state sintering to avoid potential shape loss and large deformations within the narrow range between the solid and liquidus

temperature. Therefore, from now this thesis will focus on the description of the SS processes of pre-alloyed stainless-steel powder.

The driving force for the solid-state sintering of metal particles is the reduction of the free surface energy of the system. This driving force increases when the temperature of the powder increases. During solid-state sintering, the reduction of energy is achieved from the reduction of the global surface area driven by solid-state diffusion mechanisms (see Figure 3). At low temperatures, sinter necks are formed between particles (without significant densification) by the activation of surface and grain boundary diffusion. During this initial stage of sintering, an interconnected porosity is formed. These mechanisms are active during the rest of the sintering, but grain-boundary and bulk diffusion are responsible for most of the densification at high-temperature sintering. During the intermediate step of sintering, the interconnected pore surface area and volume are reduced until pores are isolated from each other. Finally, during the last stage of sintering the number of pores is reduced and pores become spherical to reduce their energy.

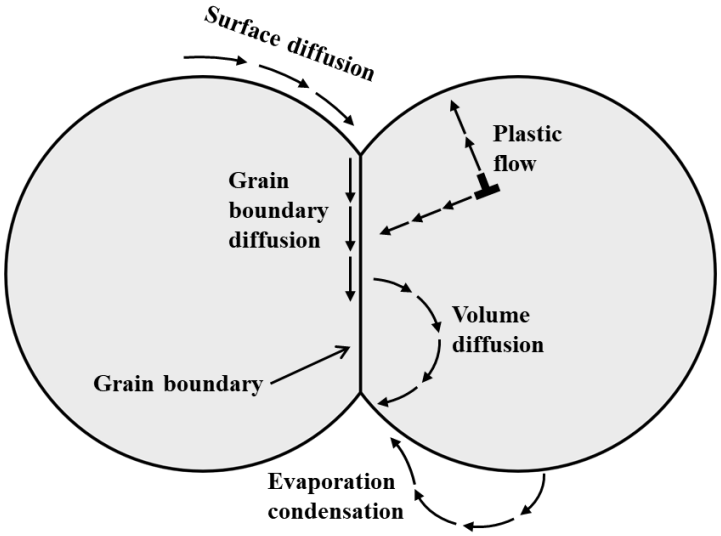

Figure 3. Schematic representation of the sintering mass transport paths, redrawn from [14].

Another important aspect of the sintering is the microstructural evolution, including the grain growth and phase transformations that may occur during the process. In general, early sintering studies clearly showed that grain growth accelerated as sintered density increased [14]. At the beginning, large pores act as big inclusions pinning grain boundaries that have slow kinetics at low temperature. As grain boundaries becomes larger and pores are annihilated, the grain growth kinetics increases. Then, pores start to become isolated from grain boundaries, reducing the grain boundary diffusion and drastically reducing densification and shrinkage.

To attain good densification during sintering, the isolation of porosity should be minimized by controlling the grain growth behavior. Due to the wide range of temperatures applied to the powder material, several phase transformations can occur during the sintering process depending on the temperature and time of sintering. In the case of steels, different transformations between BCC and FCC phases may occur before the highest sintering temperature. For instance, the δ-ferrite formation occurs at high temperatures (>1300°C depending on the alloy composition) typically used for the sintering of this material. Previous studies have shown the ability of this phase transformation to increase the sintering densification rate [8,15,16].

The atmosphere during sintering can be tuned to ensure adequate powder surface conditions during the process. They can be divided in protective or reducing atmospheres depending on how affects the powder surface. Typically, protective atmosphere consists of inert gases (N_2, Ar and He, depending on alloy system used) with low oxygen content to avoid any detrimental surface reaction with oxygen (i.e. oxidation) that would reduce or inhibit the sintering kinetics. On the other side, reducing atmospheres (H_2 and its mixes with N_2 or Ar to reduce the operating costs) allows to effectively reduce surface metal oxides, covering the metal particles, and promote bonding between the metal particles. Special attention should be put on the solubility of the gases and the reaction products into the powder material. Soluble gases can permeate through the material, but insoluble gases accumulate in the residual pores and resists densification as the pressure increases, possibly leading to swelling [17]. Therefore, the choice of atmosphere must be done considering the thermo-metallurgy of the materials together with the cost, productivity and the final properties achieved. When sintering 316L powder compacts, pure H_2 or Ar-H_2 mixtures have been widely used to reduce surfaces oxides during sintering. These atmospheres produce good results in terms of final density and properties of the sintered parts [4,18,19].

CHAPTER 3: MODELLING OF SINTERING

The initial theoretical analysis of the sintering processes was focused on the local sintering kinetics caused by the mass transport mechanisms between particles. This initial modelling attempts were generalized for the prediction of the sintering behavior. Despite the insightful concepts learned from early studies on the local sintering kinetics, several macroscopic factors were still not considered (e.g. external forces or microstructure inhomogeneities). To include these external macroscopic influences a new approach was developed based on the use of continuum mechanics, treating the powder compact as a continuum media. These models are intended for the prediction of the density and component shape evolution at the macroscale level, aiming to solve the practical problems of the sintering technology. The present thesis will focus on the continuum modelling of sintering for the prediction of components manufactured using BJT technology.

The green component obtained after the BJT printing is considered as continuum porous medium consisting of a solid and porous volume fraction. During sintering, a decrease on the porosity is produced by the sintering stress (sintering driving force) or stresses caused by external forces (e.g. gravity). This evolution is typically characterized by the relative density and/or porosity with the following relationship:

$$\theta = V_P/V_T = 1 - \rho \tag{1}$$

where V_T is the total volume, V_P the pore volume, θ the porosity and ρ the relative density.

Assuming that evaporation of solid substance and the mass of gases inside the pores are negligible, the powder compacts follow the mass conservation law during sintering. For the application to the continuum modelling, this principle can be formulated in a derivative form as follows:

$$\frac{\dot{\theta}}{(1-\theta)} = \dot{e} = tr(\dot{\boldsymbol{\varepsilon}}) \tag{2}$$

where $\dot{\theta}$ is the porosity elimination rate, ė the volumetric strain rate and tr($\dot{\boldsymbol{\varepsilon}}$) is the trace of the strain rate tensor.

Typically, constitutive relationships have been proposed by different authors to describe the inelastic strain rates caused by the sintering process. Skorohod and Olevsky developed one of the most widespread theories and model of sintering,

which was summarized with detail in the review paper [20]. This theory is based on phenomenological concept of the linear-viscous flow of porous bodies developed by Skorohod [21] and further advanced based on the generalized viscous flow concept developed by Olevsky [20]. The constitutive relationship derived by Olevsky for the general case of non-linear viscous porous materials is:

$$\boldsymbol{\sigma}_{ij} = \frac{\sigma(\mathrm{W})}{W}\left[\varphi\dot{\boldsymbol{\varepsilon}}_{ij} + \left(\psi - \frac{1}{3}\varphi\right)\dot{e}\delta_{ij}\right] + P_L\delta_{ij} \tag{3}$$

where σ(W) and W are the equivalent stress and strain rate. φ and ψ are the normalized shear and bulk viscosity. P_L is the effective sintering stress. $\dot{e}$ is the volumetric strain rate and δ_{ij} is the delta Kronecker function.

In equation (4), the left term of the equation represent the externally applied stresses. The right-hand term is the sintering stresses (driving force for sintering) and the rest represent the resistance of the material to the volumetric and shape deformation. This constitutive relationship can be used for a wide range of powder consolidation processes like spark plasma sintering (SPS) [22] or pressure-less sintering [23]. For each case, a constitutive relation can be derived from the general form by considering specific hypotheses. In this study, the case of linear-viscous behaviour of the solid material during the pressure-less isotropic sintering is considered. Therefore, the constitutive relationship has the following form:

$$\boldsymbol{\sigma}_{ij} = 2\eta_0\left[\varphi\dot{\boldsymbol{\varepsilon}}_{ij} + \left(\psi - \frac{1}{3}\varphi\right)\dot{e}\delta_{ij}\right] + P_L\delta_{ij} \tag{4}$$

where η_0 is the shear viscosity of the powder material (solid phase).

The solid material shear viscosity η_0 has been described by different functions in the literature (polynomial and exponential functions). In metallic polycrystalline materials, the sintering is driven by thermally activated diffusion mechanisms. Therefore, the Arrhenius function is typically used to describe the viscosity evolution and shows good results [24]:

$$\eta_0 = A_0 T exp\left(\frac{Q}{RT}\right) \tag{5}$$

where A_0 is the pre-exponential term and Q is activation energy.

The determination of the porosity dependency of the material parameters is treated by many different authors. Therefore, several forms of the bulk and shear viscosity, and the effective sintering stress have been proposed in the literature. The normalized

expressions used by Olevsky model were derived from the analysis proposed by Skorohod [21] and have the following form:

$$\varphi = (1-\theta)^2 \tag{6}$$

$$\psi = \frac{2}{3}\frac{(1-\theta)^3}{\theta} \tag{7}$$

$$P_L = 3\alpha\frac{(1-\theta)^2}{r_0} \tag{8}$$

where α is the surface energy of the powder and r_0 is the initial particle size.

Other authors have proposed different analytical expressions for the normalized bulk modulus. For instance, the work developed by Olevsky and Tikare [25] proposed the use equation (9), where the unknown parameters c and d can be determined using regression analysis based on the minimum square deviations.

$$\psi = \frac{2}{3}\frac{(1-\theta)^c}{\theta^d} \tag{9}$$

Several studies have shown the necessity to include the effect of particle size evolution on the sintering constitutive model [26–29]. In some cases, the initial particle size r_0 is assumed to be equal to the grain size during the sintering process. Then, grain growth kinetic models can be implemented in the modelling of sintering. Traditional grain growth models can be used, but they typically overestimate the kinetics when applied to highly porous materials [14]. Olevsky proposed grain growth kinetics models that include functions of porosity to simulate the kinetics behaviour during sintering processes [30]:

$$\frac{dG}{dt} = \frac{k_0}{3G^2}\left(\frac{\rho_c}{2-\rho_c-\rho}\right)^{3/2} exp\left(\frac{-Q_G}{RT}\right) \tag{10}$$

where, G is the grain diameter, k_0 is the pre-exponential term, Q_G is the activation energy and ρ_c is a critical porosity that accounts for the transition between porosity influenced and normal grain growth.

One of the key steps of any modelling framework is the determination of the model constants that determines the specific material behaviour. Some models allow for the utilisation of physical constants (e.g. grain boundary and lattice diffusion coefficients) available in the literature [31]. But phenomenological models of sintering typically require additional determination of model constants from experimental data. The ability of dilatometry equipment to precisely measure the linear shrinkages is used for

the calculation of the volume and density evolution of specimens during sintering. Other techniques such as hot forging experiments [32] and beam bending experiments [33] have been combined with dilatometry for the estimation of parameters for sintering models. Also, when grain growth kinetics are included in the model, the microstructure should be precisely characterized to estimate the grain growth constants. The microstructural characterization is a highly time-consuming process [26], thus, some authors have proposed methodologies to estimate these constants from dilatometry data or literature values [27]. Finally, the last important step is regarding the postprocessing methodology to fit the material parameters with all the collection of experimental data obtained. Typically, the sintering constitutive relations are simplified by assuming the isotropic pressure-less sintering dilatometry conditions. When possible, a linear regression method is used for fitting the equation containing the temperature-dependent material viscosity constants [27,28,34]. However, in other cases the influence of various conditions of external fields like pressure of electric field complicates the process for the material parameters determination [29,30].

From the industrial perspective, the objective is to obtain a model with the best possible performance when it comes to the final tolerances and minimal calculation time and at the same time minimize the experimental work needed for its calibration. However, in sintering modelling these two factors are typically inversely related, and compromise between them must be achieved. In the present thesis study, the different processes available in the literature have been explored and further methodologies have been proposed based on the actual knowledge about the modelling of sintering processes.

CHAPTER 4: MATERIALS AND METHODS

4.1 Materials and manufacturing process

The samples used in this study were produced by binder jetting. Two different combinations of BJT system and 316L powder feedstock variants were used. One set of samples was produced using the ExOne Innovent+ system by using Sandvik Osprey® 316L stainless steel feedstock and will be identified as SV in this work. The other set of samples were produced using DM P2500 Binder Jetting system (Digital Metal AB) and DM 316L powder feedstock that will be identified as DM. In both cases, the standard aqueous-based organic binder provided for each BJT printing system was used.

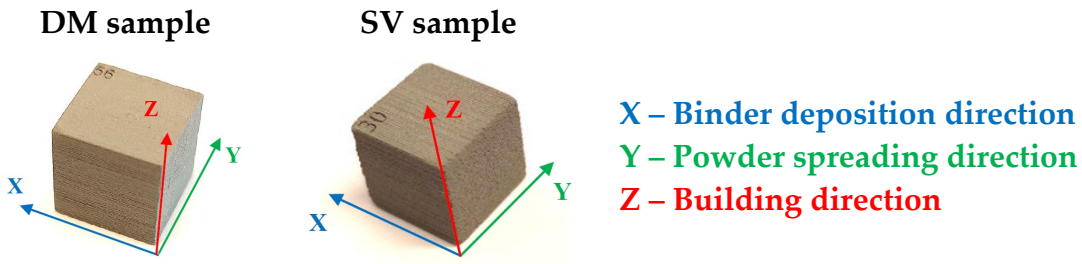

Figure 4. 10x10x10mm cubic samples printed using the different BJT systems and 316L powders.

Cubic samples with a size of 10x10x10 mm^3 were printed using both manufacturing systems. Samples were oriented in the build space with the cube's planes orthogonal to the main printing directions: building direction (Z axis), printhead movement (X axis) and recoating direction (Y axis). Consequently, distance measurements between parallel planes allows the characterization of the dimensional changes along the corresponding orthogonal axis. Each sample was designed with an identification number (ID) printed on the top surface, also used later for axis identification. After printing, the powder box was cured in an oven and samples were extracted during the depowdering process. The details of the curing and debinding step depend on the BJT system used and are described in Table 1. Lastly, some of the samples within each set were consolidated by pre-sintering in an industrial batch furnace under pure hydrogen atmosphere following 5°C/min heating rate up to 900°C with a dwell time of 1 hour and final furnace cooling down to room temperature.

Table 1 Different curing and debinding processes applied during the experimental process.

BJT System	Curing process	Debinding process
SV	**12 h at 200 °C in low vacuum achieved with a membrane pump connected to the curing furnace**	**Debinding step combined with sintering: 460°C for 2h in reducing atmosphere (H_2)**
DM	**3h at 200°C in an oven without protective atmosphere**	**Debinding at 345°C for 3h in an oven without protective atmosphere**

4.2 Material Characterization

4.2.1 Dilatometry (DIL)

Dilatometry is one of the most accurate methods for measuring dimensional change in a specimen as a function of temperature and time. These dimensional measurements are typically related to sintering densification shrinkages, thermal expansion/contraction and dimensional changes caused by microstructural phase transformations. The instrument used for the experiments is a vacuum tight dilatometer DIL 402C from NETZSCH (NETZSCH-Gerätebau GmbH, Germany) equipped with W-Re thermocouple for inert or reducing atmosphere. The horizontal push rod dilatometer is connected to displacement transducer, which converts the linear displacement into measurement signals with a high resolution of 1.25 nm/digit. The dilatometer chamber is connected to the rotary and turbo pumps in sequence allowing to perform sintering at vacuum down 10^{-5} mbar. The instrument is evacuated and flushed with argon gas up to three times before each measurement to reduce air residues. The cubic sample is supported by an alumina holder and the horizontal push rod is positioned directly against the cube's face with a force of 30 cN. All sintering trials were performed under high-purity hydrogen atmosphere (99.9999%) flowing at 100 ml min^{-1} to ensure good reduction atmosphere.

4.2.2 Metallography

Samples after sintering or pre-sintering were prepared for microstructural analysis by standard metallographic methods. The cubical samples can be cut along three different cross-sections planes defined by two of the sample's axis (i.e. XZ, YZ or XY), thus the cross-section plane will be identified for each case. Cut cross-sections were mounted, grinded and polished using a Struers Tegrapol-11 automatic system. For porosity analysis, samples were polished with up to 1 μm suspended diamond

solution. An additional step is performed when needed for each specific microstructural characterization case:

- **EBSD analysis:** final polishing step was performed using colloidal suspension of silica particles (~50 nm) on an oxide polishing cloth.
- **Grain boundaries:** Electrochemical etching with 40% nitric acid (HNO_3) solution is performed. This solution is specially used for grain size measurements due to the ability to not reveal twin boundaries.
- **Delta-ferrite phase:** Electrochemical etching with 40% sodium hydroxide (NaOH) solution is performed.

4.2.3 Light optical microscopy

Light optical microscopy (LOM) is a widely used characterization technique used within the powder metallurgy field. This methodology allows for the 2D characterization of porosity in cross-sectional images. Although the resolution is limited by the wavelength of the visible light, it is sufficient for the identification of the particles and pores formed by micron-size powder used in binder jetting manufacturing. Images of the polished samples were obtained using a Zeiss Axioscope 7 light optical microscope (LOM) equipped with Zeiss Axiocam 105 color camera. Images of the entire cross-section can be obtained by stitching high magnification images. FIJI ImageJ software was used for performing the density measurements and porosity analysis [35].

4.2.4 Scanning electron microscopy

The scanning electron microscopy (SEM) is typically used instead of LOM when higher resolution is needed. The working mechanism of SEM is based on an electron beam generated by an electron gun (field emission or W-filament) and travels through electromagnetic fields and lenses, which focus the beam down toward the sample. Then, different detectors collect the emitted radiation (X-rays) and electrons (secondary SE and backscattered BSE) ejected from the sample which are used for different analysis purposes. Electron Backscatter Diffraction (EBSD) is a modern SEM based technique to obtain qualitatively data from the internal lattice structure of the material to collect and process numerous useful information like crystalline phases, grain size, grain boundaries, crystallographic textures and local strain variations to name some. In this study, this technique will be used for the identification of microstructural phases and grain size.

A scanning electron microscope Zeiss Leo Gemini 1550 with a field emission gun (FEGSEM) was used for microstructure characterization. Grains with different lattice structures were identified by the electron backscattered diffraction (EBSD) technique and data were postprocessed by using open-source MTEX code [24]. The EBSD measurements were performed with a step size of 0.5 μm and an acceleration voltage of 20 kV. The acquired phase maps were processed after the acquisition, i.e. minor noise reduction was applied. High angle grain boundaries (twin boundaries) were defined by a misorientation of ~60° and are illustrated by white lines in the resulting maps. The misorientation value of ~60° found for the twin boundaries is typical for annealed 316L stainless steels [25]. Non-indexed data were related to the porous areas and is illustrated by black colored areas in the resulting maps.

4.2.5 Density measurements and porosity analysis

During this work, three different density measurement methods were used to evaluate the relative density of the porous samples during the binder jetting manufacturing process. The **geometry-based density** of cubical samples is obtained using sample's weight (m) and volume (V) from dimensional measurements as $\rho(\%) = \frac{\mathrm{m}}{\mathrm{V} \cdot \rho_{full}} \cdot 100$, where $\rho_{full} = 7.95\ g/cm^3$. The **LOM-based density** was obtained by dividing cross-section into 30x30 regions of interest (ROI) where the area fractional density was measured individually using image analysis. The **Archimedes density** was measured following the standard method ASTM B328. A manual caliper with a resolution of 0.01 mm and high precision balance with a resolution of 0.0001 g were used for the measurements. Then, the image analysis of the porosity morphology characteristics was done by using FIJI ImageJ particle analysis plug-in [35]. Pores with an area < 0.3 μm² (6 pixels) were excluded. The area distribution of the pores, based on the equivalent circle diameter (CED), was calculated by summing up the total pore area from each pore size class defined.

4.2.6 Chemical analysis

The chemical analysis of the BJT samples was done using combustion analysis (HFIR), melt extraction technique (EXTR) and X-ray Fluorescence Spectrometry (XRF) for elemental analysis. The C- and S content was measured using HFIR, O- and N content was measured using EXTR and the other chemical elements was measured using XRF.

CHAPTER 5: RESULTS AND DISCUSSION

In this chapter, the research questions previously defined are addressed by summarizing and discussing the results from appended manuscripts.

RQ1 is addressed by Paper I, focused on the development of an experimental study to characterize the multi-axial dimensional evolution of BJT 316L. RQ2 is partially addressed by Paper II by the characterization and analysis of the microstructure evolution during sintering. Finally, Paper III is focused on the development of a simulation model to include the effect of the δ-ferrite phase transformation during the sintering of 316L at elevated temperatures.

5.1 Sintering anisotropy of 316L BJT samples

Because of the inherent characteristics of the BJT printing process (e.g. the layer-by-layer printing), the printed components may exhibit some degree of dimensional and microstructural anisotropy during the debinding and sintering stage. This anisotropy has been frequently reported in previous literature [2,3,10,36–40], showing larger shrinkages along the building direction (Z axis). This anisotropy is commonly attributed to the presence of a "layered" porous green structure induced by the BJT printing. This section presents and discuss the results from a detailed characterization of the sintering evolution of 316L BJT samples along the different printing directions. First, the details of the dimensional evolution were explored. Second, the microstructural evolution was characterized and discussed.

5.1.1 Multi-axial dimensional evolution during sintering (Paper I)

The motivation for Paper I was to analyse in detail the evolution of the dimensional anisotropy during the debinding and sintering process. For that, dilatometry sintering experiments were performed using green and pre-sintered cubic samples. Two different sintering cycles were used with different heating rate (5°C/min and 10 °C/min) and isothermal temperatures (1300°C and 1370°C) with 60 min dwell time. Finally, each designed sintering experiment was repeated along each cube orthogonal direction. These directional axes were intentionally aligned to the BJT printing directions, where Z is the building direction, Y is the powder recoating direction and X is the direction of the printhead movement (binder deposition).

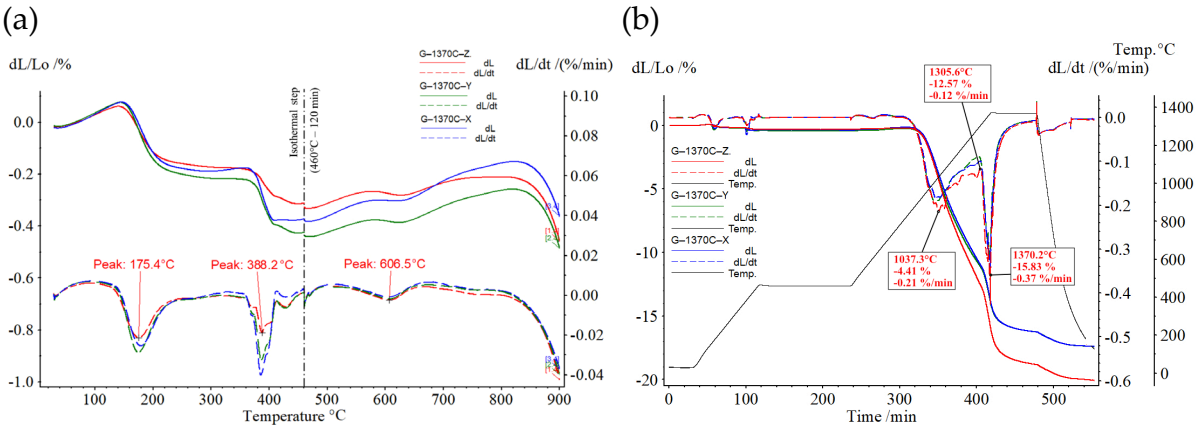

Figure 5. Multi-axial sintering results from dilatometry sintering along the X (blue), Y (green) and Z (red) axis: (a) zoom in the data below 900°C for details on debinding step performed and (b) full sintering curves obtained from the dilatometry test at 5°C/min up to 1370°C on green samples. (SV samples results)

Figure 5 (a) shows very low shrinkages (<0.5%) and nearly isotropic dimensional evolution during debinding of the SV samples. The shrinkage kinetics can be directly connected with the binder burnout process, where each stage temperature range agrees with results reported previously in [10]. Shrinkages occurring during debinding can be related to the rearrangement of particles. Figure 5 (b) shows larger shrinkages along the building direction (Z axis) for the SV samples set. This conclusion is valid for all the sintering cycles investigated in Paper I. However, the degree of anisotropy is not a constant but develops during sintering. Then, two anisotropic factors K_Y and K_X were calculated (see Figure 6), which increase up to a final value of ~1.15 for all the cycles studied. However, K values are stabilized before the isothermal step for sintering at 5 °C/min while for sintering at 10 °C/min these factors are progressing during the whole sintering cycle. These results indicate that dimensional anisotropy evolution depends on the evolution of the pore distribution anisotropy driven by the diffusion phenomena occurring during the sintering process.

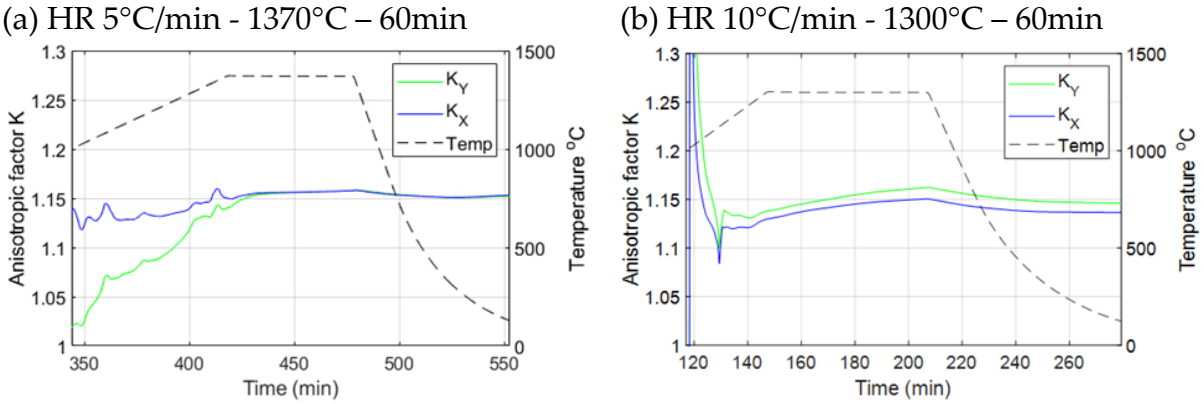

Figure 6. Anisotropic factors calculated from shrinkage dilatometry data: (a) sintering at 5°C/min up to 1370°C for 60min and (b) sintering at 10°C/min up to 1300°C for 60min (SV samples results).

Additionally, the anisotropy has been characterized by measuring the final shrinkage using a caliper. Figure 7 (a) shows the shrinkages for each samples set and (b) the anisotropy factors derived from these values. When comparing shrinkages measured along X and Y directions, the general trend shows that shrinkages along X direction are slightly larger (less than 0.5% absolute difference). Besides, averaged K_Y and K_X from manually measured values are 1.16±0.03 and 1.13±0.03, respectively, which agree with the final values obtained from dilatometry.

(a) Final shrinkages (b) Anisotropy factors

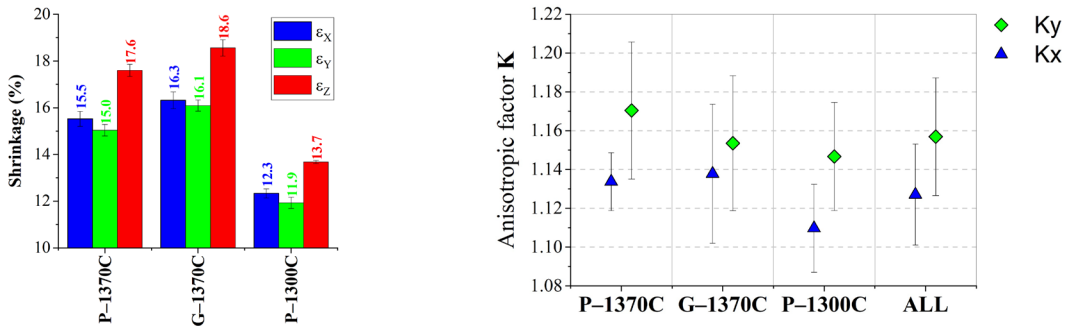

Figure 7. Data calculated from calliper dimensional measurements of the BJT samples studied: (a) sintered averaged shrinkages of the sintered samples along each direction and (b) averaged anisotropic factors calculated from the sintered shrinkage measurements. (SV samples results).

Similar anisotropy factors can be derived from the shrinkage values reported in the literature [10,36,37,39]. These studies suggest that the anisotropy is particularly affected by the powder PSD and some printing parameters (e.g. layer thickness). Also, the type of spreading system (e.g. blades or roller) used influences the powder arrangement during the spreading process. In the next section the influence of these variables on the initial green microstructure, the sintering, and its relationship with the potential anisotropy evolution will be discussed.

5.1.2 Microstructural evolution during sintering (Paper II)

Figure 8 shows the density values obtained by the methods defined in section 4.2.5 . In general, LOM-based density results from different cross-sections are relatively similar, but typically higher than geometry-based and Archimedes density measurement results. Archimedes and geometry-based measurements are considered more accurate because it quantifies the density within the whole sample volume. Archimedes density ~1% higher than geometry-based density may be caused by the omitted surface roughness effect when measuring the volume with a caliper.

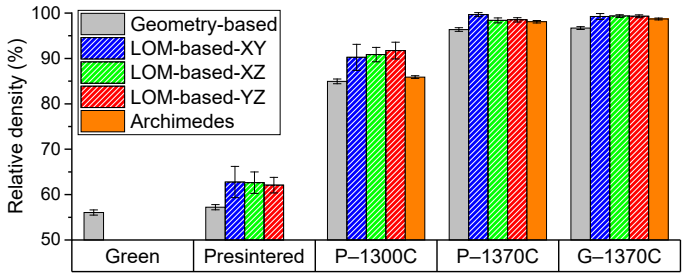

Figure 8. Relative densities calculated by the three different methods described in section 4.2.5. (SV samples results).

During sintering of BJT components, the initial interconnected porosity of green samples transitions to small isolated equiaxial pores for samples sintered near to full density. Also, the images in Figure 9 reveal the potential anisotropic porous structure evolution of the BJT samples. Also, the statistical analysis of the individual pore characteristics (i.e. size, aspect ratio and circularity) from Paper II revealed a bimodal distribution related to the presence of layers with different porosity features that evolves during the sintering process. Then, EBSD analysis was performed to reveal the phases present on the sintered microstructure. Figure 10 reveals the presence of δ delta-ferrite BCC phase on the sample sintered at 1370°C. The boosted densification detected by dilatometry (see section 5.1.1) is related to this transformation via two mechanisms: the increased self-diffusion rate of the BCC (δ delta-ferrite) compared with the FCC (γ austenite) and the formation of new grain boundaries [8,16,41,42].

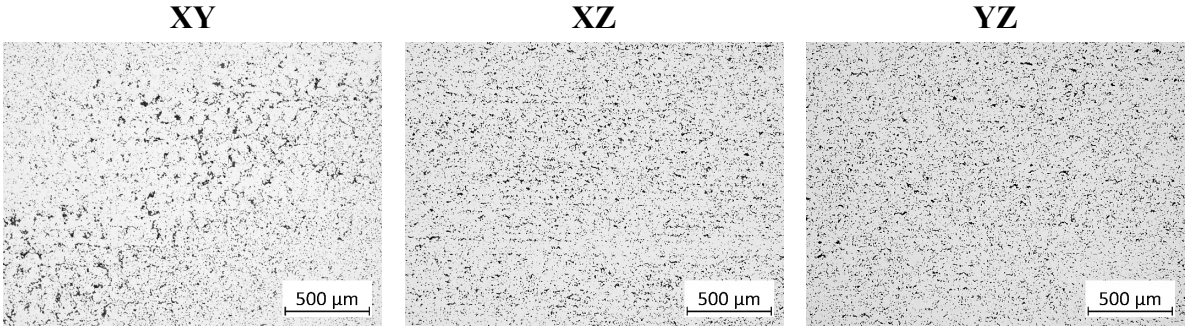

Figure 9. XY, XZ and YZ cross-section LOM images from samples sintered up to 1300°C. (SV samples results).

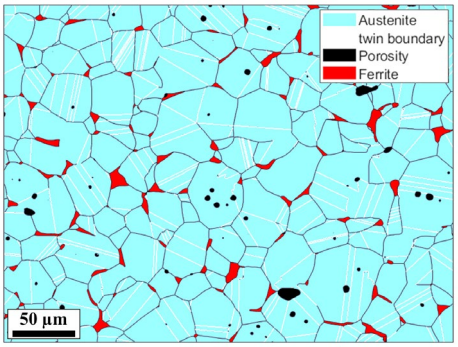

Figure 10. EBSD phase map of the sample sintered at 1370°C for 60 min. (SV samples results).

5.2 Effect of δ-ferrite transformation on the modelling of sintering behaviour of 316L binder jetted components (Paper III)

The work included in Paper III developed a new way to introduce the delta-ferrite phase transformation effects on the material shear viscosity. The equation for porosity evolution during sintering was derived from the continuum theory of sintering [20] applied to the case of linear-viscous material during isotropic pressure-less sintering:

$$\dot{\theta} = -\frac{9\alpha\theta^{0.64}(1-\theta)^3}{2G\eta_0(1-\theta)^{11.55}} \tag{11}$$

where α is the specific surface energy and η_0 is the shear viscosity of the porous body's skeleton material. Besides, the average grain size evolution was predicted using the following grain growth kinetic equation [30]:

$$\frac{dG}{dt} = \frac{k_0}{3G^2}\left(\frac{\theta_c}{\theta_c+\theta}\right)^{3/2} exp\left(\frac{-Q}{RT}\right) \tag{12}$$

where $k_0 = 29.65e-13\ \mu m^3 s^{-1}$, $Q = 164.8\ kJ$, and $\theta_c = 0.0514$.

From equation (11), the solid material viscosity can be derived as follow:

$$\eta_0 = -\frac{-9\alpha\theta^{0.64}(1-\theta)^3}{2G\dot{\theta}(1-\theta)^{11.55}} \tag{13}$$

Therefore, the porosity evolution obtained by dilatometry sintering experiments were used to estimate the viscosity evolution during sintering. Experiments were performed using the pre-sintered DM cubic samples at different heating rates of 2, 5 and 15 °C/min up to 1370°C with a dwell time of 60 min. In this case, the measured shrinkages along different directions were relatively analogous (variation ≲ 1%) and the sintering isotropic assumption can be used for modelling.

(a) (b)

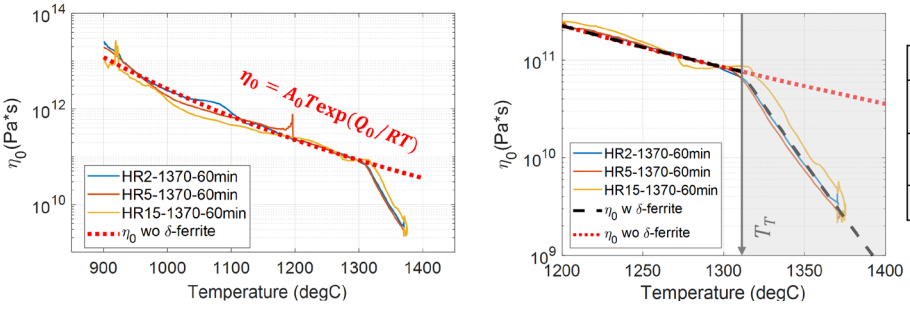

Parameter	$i = 1$	$i = 2$
A_i/α $[s\,m^{-1}K^{-1}]$	8.993	5.335e-32
Q_i $[K\,J\,mol^{-1}]$	201.7	1178.7
T_T $[K]$	1583.62	

Figure 11. (a) η_0 calculated by equation (9) using experimental data and (b) new piecewise Arrhenius function fitted to the experimental data and values of fitted constats. (DM samples results).

Figure 11(a) shows the skeleton material viscosity calculated from the experimental data, where the overlapping of the different curves can be observed. This confirms that η_0 is a material and temperature-dependent parameter as defined in [20]. Typically, Arrhenius equation is used for describing η_0 as a function of temperature. However, curves obtained diverge after a temperature ~1310°C from the Arrhenius curve (dotted red curve in Figure 11). During sintering above this temperature, microstructural changes are caused by the δ-ferrite phase formation. Therefore, a new skeleton material viscosity function was defined to account for this effect. Therefore, the following piecewise function with four material constants was proposed:

$$\eta_0 = A_i T\, exp\left(\frac{Q_i}{RT}\right) \begin{cases} i = 1 \rightarrow A_1\, Q_1, & if\ T < T_T \\ i = 2 \rightarrow A_2\, Q_2, & if\ T \geq T_T \end{cases}$$
$$where: T_T = \frac{Q_2 - Q_1}{R\, ln\left(\frac{A_1}{A_2}\right)} \qquad (14)$$

where a transition temperature T_T was introduced to ensure the continuity of the function within the temperature domain and is directly related to the δ-ferrite transformation temperature. The proposed η_0 function is compared with the traditional Arrhenius function and experimental data in Figure 11(b). The piecewise η_0 expression describes with excellent accuracy the effect of δ-ferrite transformation during sintering. Also, the kinetic effect of the phase transformation can be neglected for the range of heating rates studied. However, a slight deviation of the 15HR curve indicates that this assumption may not be valid for higher heating rates.

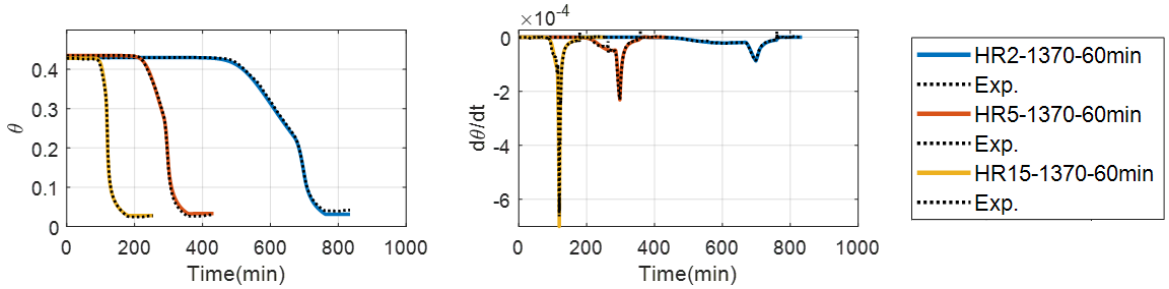

Figure 12. Porosity evolution during sintering: experiment (dotted lines) against simulation results.

Finally, the model developed was used to predict the density evolution during the thermal profile followed by the dilatometry experiments at different heating rates. Figure 12 shows the comparison between the model and experimental data for each case studied. These results show an excellent performance of the model to predict the density evolution during the complete sintering cycle. In particular, the shrinkage rate increase caused by the δ-ferrite transformation was accurately reproduced for all the cases studied in this study.

CHAPTER 6: CONCLUSIONS

The research that is provided in this thesis leads to the following findings:

- Different levels of anisotropy shrinkage behavior were observed (K=1.05 – 1.17), with larger shrinkage along the building direction (Z-axis). The anisotropy level may vary depending on different factors like the printer system and powder particles characteristics.
- The multiaxial dilatometry experiments revealed a continuous development of the anisotropy during the sintering cycle, which was driven by the densification caused by the sintering mass transport mechanisms. An anisotropic factor of ~1.15 was derived from shrinkage measurements in the SV samples.
- Shrinkage during debinding (~0.5%) is insignificant compared to the final sintered shrinkages. Such shrinkage may be caused by slight rearrangement of powder particles during binder burnout. Also, no anisotropy in shrinkage was observed during the debinding step.
- A rapid increase in shrinkage rate and densification was observed from dilatometry and microstructural analysis of 316L BJT samples sintered up to 1370°C. This behavior was related to the δ-ferrite transformation occurring at high temperatures above ~1310°C.
- Density of samples at different states was measured by different methods. Geometry-based and Archimedes method showed the best accuracy and consistency for the density characterization at different density levels. Close to full density (~98%) was obtained from green samples (~56.1%) when sintering at 1370°C.
- Image analysis of the microstructure showed the solid volume fraction increase during sintering. Also, anisotropy of pore sizes and distribution was revealed by statistical analysis of different cross-sections pores. Pore area-size distribution within XY cross-sections was noticeably different (heterogeneous distribution) which was related to the interlayered porous structure induced during BJT printing.

Finally, this thesis includes the initial development of a numerical model for the simulation of the sintering process of 316L stainless steel BJT components. The new model proposed was based on the linear-viscous case from the continuum theory of sintering applied to the typical pressure-less sintering process of BJT components. In this thesis work, the model development was focused on including the effect of δ-ferrite transformation in the densification behavior during sintering. The modelling work presented leads to the following findings:

- The analysis of the material shear viscosity evolution calculated from dilatometry experiments was used to propose a new Arrhenius-like piecewise function to describe its behaviour. Then, the required viscosity constants (A_0/α and Q) were obtained by fitting to the experimental data.
- A transition temperature was included in the material viscosity function, which is directly related to the value from thermodynamic calculations. Also, the effect of the transformation kinetics can be omitted for the range of heating rates studied (2-15°C/min).
- The density evolution calculated from the model demonstrated a good precision when compared to the experimental data. Specially, the increased densification rate caused by the δ-ferrite transformation was clearly reproduced.

CHAPTER 7: FUTURE WORK

A detailed characterization methodology of the BJT sintering step process was developed by combining dilatometry and microstructural characterization. Two different BJT printing technologies and 316L powders were used in different sections of the thesis. Also, a baseline for the sintering modelling methodology was introduced in this work initially assuming isotropic sintering behavior. However, different aspects of the manufacturing and sintering process are not yet considered and will be studied in the future:

- Implementation of the developed sintering model in a finite element method (FEM) software for the simulation of components with complex geometries susceptible to significant shape deformations under different external forces (e.g. gravity or friction).
- Study the potential impact of the powder characteristics (e.g. powder size distribution) and/or the printing process in the identification of the model parameters and its impact on the simulation results.
- Study the effect of variations on the stainless-steel chemistry on the modelling methodology proposed. This will be done by combining the continuum model of sintering and thermodynamic simulations to predict the effect on the phase evolution during sintering.
- Expanding the model proposed to the anisotropic case, where shrinkages along different printing directions was detected during the experimental characterization. Also, potential effect on the anisotropy of shape deformation will be further studied experimentally and included in the modelling approach.
- Perform a high-resolution analysis of the complex porosity evolution of samples produced by BJT. An advanced non-destructive characterization technique like X-Ray computed tomography will be used for this objective. This will allow for a precise 3D characterization not viable by traditional methods.
- The modelling of sintering was initially developed in this thesis for the BJT manufacturing of 316L. Its expansion to other alloys systems in BJT as well as other AM and PM technologies as e.g. lithography-based metal additive manufacturing and MIM will be further studied.

References

[1] ASTM International, ISO/ASTM52900-21 Standard Terminology for Additive Manufacturing – General Principles – Terminology, West Conshohocken, PA; ASTM International. (2021). http://www.ciri.org.nz/nzrma/technologies.html.

[2] A. Mostafaei, A.M. Elliott, J.E. Barnes, F. Li, W. Tan, C.L. Cramer, P. Nandwana, M. Chmielus, Binder jet 3D printing—Process parameters, materials, properties, modeling, and challenges, Prog Mater Sci. 119 (2021) 100707. https://doi.org/10.1016/j.pmatsci.2020.100707.

[3] Y. Lee, P. Nandwana, S. Simunovic, Powder spreading, densification, and part deformation in binder jetting additive manufacturing, Progress in Additive Manufacturing. (2021). https://doi.org/10.1007/s40964-021-00214-1.

[4] S. Mirzababaei, S. Pasebani, A Review on Binder Jet Additive Manufacturing of 316L Stainless Steel, Journal of Manufacturing and Materials Processing. 3 (2019) 82. https://doi.org/10.3390/jmmp3030082.

[5] A. Lores, N. Azurmendi, I. Agote, E. Zuza, A review on recent developments in binder jetting metal additive manufacturing: materials and process characteristics, Powder Metallurgy. 62 (2019) 267–296. https://doi.org/10.1080/00325899.2019.1669299.

[6] International ASTM, Standard Test Method for Tap Density of Metal Powders and Compounds B527 − 22, B527. (2015) 15–18. https://doi.org/10.1520/B0527-22.2.

[7] N.D. Parab, J.E. Barnes, C. Zhao, R.W. Cunningham, K. Fezzaa, A.D. Rollett, T. Sun, Real time observation of binder jetting printing process using high-speed X-ray imaging, Sci Rep. 9 (2019) 1–10. https://doi.org/10.1038/s41598-019-38862-7.

[8] Y. Wu, R.M. German, D. Blaine, B. Marx, C. Schlaefer, Effects of residual carbon content on sintering shrinkage, microstructure and mechanical properties of injection molded 17-4 PH stainless steel, J Mater Sci. 37 (2002) 3573–3583. https://doi.org/10.1023/A:1016532418920.

[9] E. Hryha, L. Nyborg, A. Malas, S. Wiberg, S. Berg, Carbon control in PM sintering: Industrial applications and experience, Powder Metallurgy. 56 (2013) 5–10. https://doi.org/10.1179/0032589912Z.00000000085.

[10] N. Lecis, M. Mariani, R. Beltrami, L. Emanuelli, R. Casati, M. Vedani, A. Molinari, Effects of process parameters, debinding and sintering on the microstructure of 316L stainless steel produced by binder jetting, Materials Science and Engineering A. 828 (2021) 142108. https://doi.org/10.1016/j.msea.2021.142108.

[11] R.M. German, History of Sintering, Sintering: From Empirical Observations to Scientific Principles. (2014) 13–40. https://doi.org/10.1016/b978-0-12-401682-8.00002-1.

[12] R.M. German, P. Suri, S.J. Park, Review: Liquid phase sintering, J Mater Sci. 44 (2009) 1–39. https://doi.org/10.1007/s10853-008-3008-0.

[13] R.M. German, Supersolidus liquid-phase sintering of prealloyed powders, Metall Mater Trans A Phys Metall Mater Sci. 28 (1997) 1553–1567. https://doi.org/10.1007/s11661-997-0217-0.

[14] R.M. German, Coarsening in sintering: Grain shape distribution, grain size distribution, and grain growth kinetics in solid-pore systems, Critical Reviews in Solid State and Materials Sciences. 35 (2010) 263–305. https://doi.org/10.1080/10408436.2010.525197.

[15] R.W.K. Honeycombe, Some factors influencing the sintering behaviour of austenitic stainless steel powders, Powder Metallurgy. 20 (1977) 191–198. https://doi.org/10.1179/pom.1977.20.4.191.

[16] B. Berginc, Z. Kampus, B. Sustarsic, Influence of feedstock characteristics and process parameters on properties of MIM parts made of 316L, Powder Metallurgy. 50 (2007) 172–183. https://doi.org/10.1179/174329007X164862.

[17] R.M. German, Thermodynamic and Kinetic Treatments, 2014. https://doi.org/10.1016/b978-0-12-401682-8.00007-0.

[18] R.P. Koseski, P. Suri, N.B. Earhardt, R.M. German, Y.S. Kwon, Microstructural evolution of injection molded gas- and water-atomized 316L stainless steel powder during sintering, Materials Science and Engineering A. 390 (2005) 171–177. https://doi.org/10.1016/j.msea.2004.08.002.

[19] J.P. Choi, G.Y. Lee, J. Il Song, W.S. Lee, J.S. Lee, Sintering behavior of 316L stainless steel micro-nanopowder compact fabricated by powder injection molding, Powder Technol. 279 (2015) 196–202. https://doi.org/10.1016/j.powtec.2015.04.014.

[20] E.A. Olevsky, Theory of sintering: From discrete to continuum, Materials Science and Engineering R: Reports. 23 (1998) 41–100. https://doi.org/10.1016/S0927-796X(98)00009-6.

[21] V.V. Skorohod, Rheological basis of the theory of sintering, (1972).

[22] C. Manière, L. Durand, A. Weibel, C. Estournès, Spark-plasma-sintering and finite element method: From the identification of the sintering parameters of a submicronic α-alumina powder to the development of complex shapes, Acta Mater. 102 (2016) 169–175. https://doi.org/10.1016/j.actamat.2015.09.003.

[23] E. Torresani, R.M. German, R. Huff, E.A. Olevsky, Influence of gravity on sintering of 3D-printed powder components, Journal of the American Ceramic Society. (2021). https://doi.org/10.1111/jace.18056.

[24] M.W. Reiterer, K.G. Ewsuk, J.G. Argüello, An arrhenius-type viscosity function to model sintering using the Skorohod-Olevsky viscous sintering model within a finite-element code, Journal of the American Ceramic Society. 89 (2006) 1930–1935. https://doi.org/10.1111/j.1551-2916.2006.01041.x.

[25] E.A. Olevsky, V. Tikare, T. Garino, Multi-scale study of sintering: A review, Journal of the American Ceramic Society. 89 (2006) 1914–1922. https://doi.org/10.1111/j.1551-2916.2006.01054.x.

[26] G. Kerbart, C. Manière, C. Harnois, S. Marinel, Predicting final stage sintering grain growth affected by porosity, Appl Mater Today. 20 (2020). https://doi.org/10.1016/j.apmt.2020.100759.

[27] C. Manière, S. Chan, G. Lee, J. McKittrick, E.A. Olevsky, Sintering dilatometry based grain growth assessment, Results Phys. 10 (2018) 91–93. https://doi.org/10.1016/j.rinp.2018.05.014.

[28] C. Manière, G. Lee, J. McKittrick, S. Chan, E.A. Olevsky, Modeling zirconia sintering trajectory for obtaining translucent submicronic ceramics for dental implant applications, Acta Mater. 188 (2020) 101–107. https://doi.org/10.1016/j.actamat.2020.01.061.

[29] C. Manière, C. Harnois, S. Marinel, Porous stage assessment of pressure assisted sintering modeling parameters: a ceramic identification method insensitive to final stage grain growth disturbance, Acta Mater. 211 (2021) 116899. https://doi.org/10.1016/j.actamat.2021.116899.

[30] E.A. Olevsky, C. Garcia-Cardona, W.L. Bradbury, C.D. Haines, D.G. Martin, D. Kapoor, Fundamental aspects of spark plasma sintering: II. Finite element analysis of scalability, Journal of the American Ceramic Society. 95 (2012) 2414–2422. https://doi.org/10.1111/j.1551-2916.2012.05096.x.

[31] A. Al-Qudsi, M. Kammler, A. Bouguecha, C. Bonk, B.A. Behrens, Comparison between different numerical models of densification during solid-state sintering of pure aluminium powder, Production Engineering. 9 (2014) 11–24. https://doi.org/10.1007/s11740-014-0574-7.

[32] R. Zuo, E. Aulbach, J. Rödel, Experimental determination of sintering stresses and sintering viscosities, Acta Mater. 51 (2003) 4563–4574. https://doi.org/10.1016/S1359-6454(03)00293-3.

[33] S.H. Lee, G.L. Messing, D.J. Green, Bending creep test to measure the viscosity of porous materials during sintering, Journal of the American Ceramic Society. 86 (2003) 877–882. https://doi.org/10.1111/j.1151-2916.2003.tb03391.x.

[34] C. Manière, L. Durand, A. Weibel, C. Estournès, A predictive model to reflect the final stage of spark plasma sintering of submicronic α-alumina, Ceram Int. 42 (2016) 9274–9277. https://doi.org/10.1016/j.ceramint.2016.02.048.

[35] J. Schindelin, I. Arganda-Carreras, E. Frise, V. Kaynig, M. Longair, T. Pietzsch, S. Preibisch, C. Rueden, S. Saalfeld, B. Schmid, J.-Y. Tinevez, D.J. White, V. Hartenstein, K. Eliceiri, P. Tomancak, A. Cardona, Fiji: an open-source platform for biological-image analysis, Nature Methods 2012 9:7. 9 (2012) 676–682. https://doi.org/10.1038/nmeth.2019.

[36] B. Barthel, S.B. Hein, C. Aumund-Kopp, F. Petzoldt, Influence of Particle Size Distribution in Metal Ber Jetting – Effects on the Properties of Green and Sintered Parts, in: Procedia EuroPM 2019: International Powder Metallurgy Congress and Exhibition, 2019.

[37] A. Mostafaei, P. Rodriguez De Vecchis, I. Nettleship, M. Chmielus, Effect of powder size distribution on densification and microstructural evolution of binder-jet 3D-printed alloy 625, Mater Des. 162 (2019) 375–383. https://doi.org/10.1016/j.matdes.2018.11.051.

[38] M. Zago, N.F.M. Lecis, M. Vedani, I. Cristofolini, Dimensional and geometrical precision of parts produced by binder jetting process as affected by the anisotropic shrinkage on sintering, Addit Manuf. 43 (2021) 102007. https://doi.org/10.1016/j.addma.2021.102007.

[39] D. Huber, L. Vogel, A. Fischer, The effects of sintering temperature and hold time on densification, mechanical properties and microstructural characteristics of binder jet 3D printed 17-4 PH stainless steel, Addit Manuf. 46 (2021) 102114. https://doi.org/10.1016/j.addma.2021.102114.

[40] M. Ziaee, E.M. Tridas, N.B. Crane, Binder-Jet Printing of Fine Stainless Steel Powder with Varied Final Density, JOM. 69 (2017) 592–596. https://doi.org/10.1007/s11837-016-2177-6.

[41] H. Miyanaji, N. Momenzadeh, L. Yang, Effect of powder characteristics on parts fabricated via binder jetting process, Rapid Prototyp J. 25 (2019) 332–342. https://doi.org/10.1108/RPJ-03-2018-0069.

[42] I.D. Jung, S. Ha, S.J. Park, D.C. Blaine, R. Bollina, R.M. German, Two-Phase Master Sintering Curve for 17-4 PH Stainless Steel, Metall Mater Trans A Phys Metall Mater Sci. 47 (2016) 5548–5556. https://doi.org/10.1007/s11661-016-3687-0.